






Geophysical Research Letters[®]



RESEARCH LETTER

10.1029/2023GL102826

Extensional Earthquakes in the Absence of Magma in Northern Afar: Insights From InSAR

Alessandro La Rosa¹ , Martina Raggiunti² , Carolina Pagli¹ , Derek Keir^{2,3} , Hua Wang⁴ , and Atalay Ayele⁵

¹Department of Earth Sciences, University of Pisa, Pisa, Italy, ²Department of Earth Sciences, University of Florence, Florence, Italy, ³School of Ocean and Earth Science, University of Southampton, Southampton, UK, ⁴College of Natural Resources and Environment, South China Agricultural University, Guangzhou, China, ⁵Institute of Geophysics, Space Science and Astronomy, Addis Ababa University, Addis Ababa, Ethiopia

Key Points:

- A seismic sequence with a M_w 5.5 mainshock occurred in the Bada region of northern Afar rift between 26 and 28 December 2022
- InSAR models and seismicity revealed co-seismic deformation along conjugate faults with no involvement of magma motions
- Our observations show that extension can be achieved through purely tectonic processes in magma-rich continental rifts

Supporting Information:

Supporting Information may be found in the online version of this article.

Correspondence to:

A. La Rosa,
alessandro.larosa@dst.unipi.it

Citation:

La Rosa, A., Raggiunti, M., Pagli, C., Keir, D., Wang, H., & Ayele, A. (2023). Extensional earthquakes in the absence of magma in northern Afar: Insights from InSAR. *Geophysical Research Letters*, 50, e2023GL102826. <https://doi.org/10.1029/2023GL102826>

Received 10 JAN 2023
Accepted 2 MAY 2023

Abstract In magma-rich rifts, normal faulting is commonly thought to be induced by dike intrusions. However, whether fault slip occurs purely tectonically is unclear. An earthquake sequence starting with a M_w 5.5 earthquake occurred in December 2022 in northern Afar, a continental rift near breakup. InSAR measurements show that seismicity was caused by normal faulting alone, without involvement of magma movements. Our best-fit InSAR models show that conjugate faults ruptured during the seismic sequence with mainly normal dip-slip and total deformation corresponding to a M_w 5.7 event, in agreement with local seismic recordings. Our models show that tectonic faulting accommodates 26 cm of extension corresponding to ~30 years of plate spreading without any link to magma. Our observations point toward significant along-rift variation in the proportion of extension from faulting, potentially caused by along-rift variations in rate of extension and/or from a spatially and temporally segmented supply of magma.

Plain Language Summary The Earth's continents move away from each other forming a rift valley between the two separating tectonic plates. In mature stages of the continental rupture process, it is commonly accepted that plate separation occurs from the migration of molten rock (magma) toward the Earth's surface in narrow zones beneath the rift valley. Brittle faulting of the plate was thought to be less important. In this study we analyze the recent earthquake sequence of 26–28 December 2022 in the volcanically active northern Afar rift of Ethiopia. We show that, while the sequence occurred within the rift valley, it was caused by pure faulting without any involvement of magma migrations. These observations are unexpected and show that faults alone can assist plate separation even in mature and magma-rich rift valleys.

1. Introduction

Recent observations from geology, geodesy and seismicity at magma-rich continental rifts suggest that dike intrusion is the primary mechanism achieving plate extension (Ebinger et al., 2010; Sigmundsson et al., 2015; Wright et al., 2012). In these settings most medium-to-large magnitude, normal slip earthquakes are induced by dikes, while purely tectonic normal faulting is less common (Ebinger et al., 2010). For example, in the magma-rich rifts of Ethiopia (Afar and the Main Ethiopian rift) all the geodetically measured examples of normal faulting (i.e., since the onset of InSAR measurements in the area in 1994) have been induced by dike intrusion (e.g., Nobile et al., 2012; Wright et al., 2012).

An earthquake sequence with a mainshock-aftershocks pattern occurred between 26 and 28 December 2022 in northern Afar (Bada region), with several earthquakes recorded globally. The National Earthquake Information Center (NEIC) recorded an earthquake M_w 5.5 on 26 December at 12:21:07 (UTC), followed by a second mb 4.6 earthquake at 16:27:13 (UTC) on the same day, and a mb 4.9 at 16:14:57 (UTC) on 28 December (Figure 1). The European Mediterranean Seismological Center (EMSC) recorded the mainshock on 26 December with mb 5.2 and the second earthquake as mb 4.6, similar to the NEIC. On 28 December the EMSC recorded two earthquakes that were not detected by NEIC, both mb 4.5, at 14:02:27 (UTC) and at 14:35:19 (UTC), respectively, and later a mb 4.9 earthquake, the same as the M_w 4.9 recorded by NEIC (Figure 1). The focal mechanism of the M_w 5.5 earthquake calculated by the Global Centroid Moment Tensor (gCMT) project showed mainly normal faulting on a NNW-SSE striking plane, and with a minor component of strike-slip (Figure 1).

© 2023. The Authors.

This is an open access article under the terms of the [Creative Commons Attribution License](https://creativecommons.org/licenses/by/4.0/), which permits use, distribution and reproduction in any medium, provided the original work is properly cited.

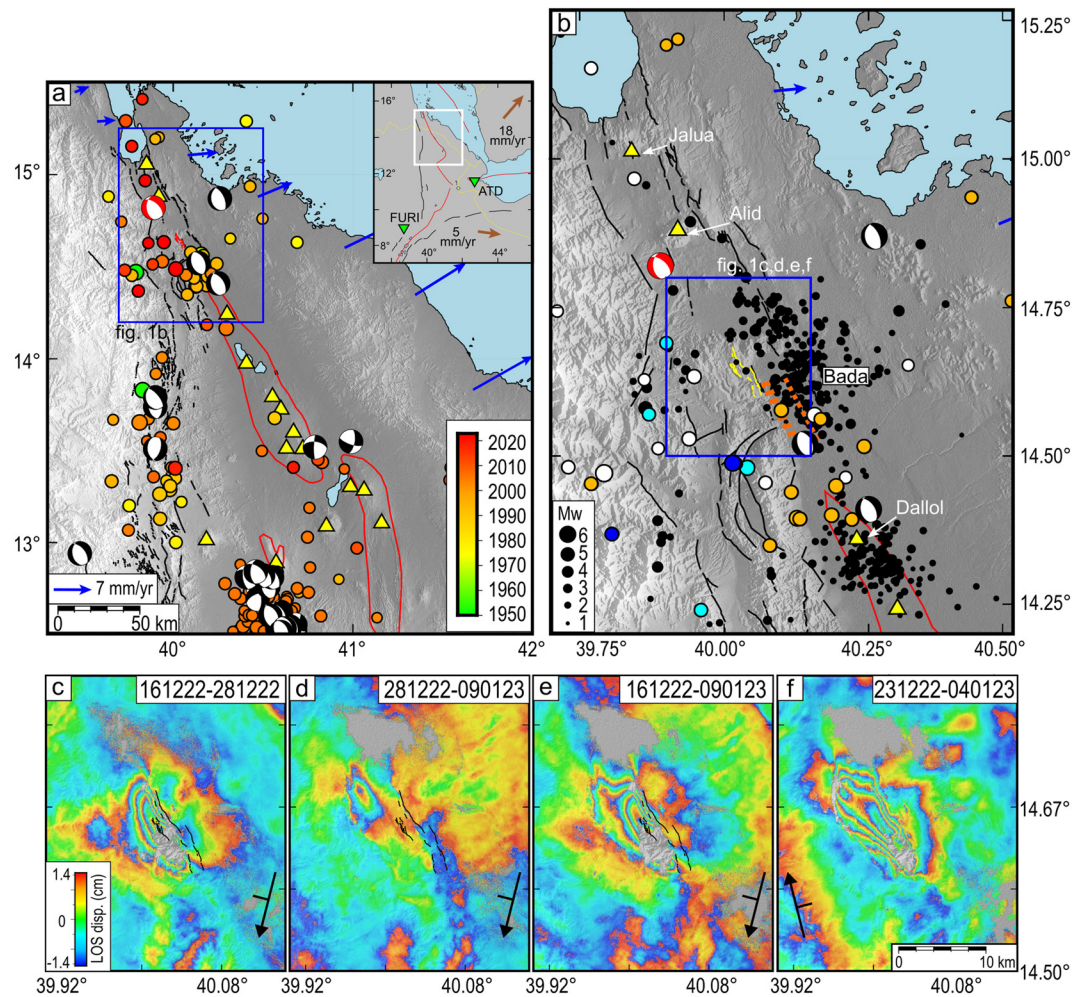


Figure 1. Map of Afar and co-seismic InSAR data set. (a) Seismicity 1950–2022 (National Earthquake Information Center, NEIC) and focal mechanisms from Global Centroid Moment Tensor 1976–2022. The red focal mechanism is the M_w 5.5 earthquake of 26 December 2022. Yellow triangles are volcanoes. Blue vectors are GPS velocities w.r.t. fixed Nubia (Viltres et al., 2020). Black lines are major faults from Zwaan et al. (2020). The inset in (a) shows the plate boundaries with spreading vectors and global seismic stations FURI and ATD as green inverted triangles. (b) shows the seismicity from NEIC as white dots, with two different locations for the December 2022 earthquakes from NEIC (blue) and European Mediterranean Seismological Center (cyan). The 1993 seismic swarm from NEIC is shown with the orange dots, as in (a). Black dots are earthquakes recorded during 2011–2013 by temporary networks (Illsley-Kemp et al., 2018). Yellow lines are faults in the area of the 2022 sequence, orange dashed lines are fractures reported by Ruch et al. (2021). (c–e) wrapped co-seismic interferograms for the initial part (c), later (d) part, and entire (e, f) seismic sequence. Positive values indicate range increase between the ground and the satellite Line-of-Sight (LOS). Black lines are faults.

Afar is an evolved continental rift formed from plate extension during the last ~ 30 Myr (Wolfenden et al., 2005), with the region including a rift-rift-rift triple junction and several microplates. In northern Afar, extension since ~ 11 Ma has been between the Nubian plate and the Danakil microplate in a NE-SW direction (Eagles et al., 2002). Currently, GPS measurements show that the spreading rates between Nubia and the Danakil microplate progressively increase southward from ~ 6 mm/yr in northern Afar (at latitude $\sim N15^\circ$) where the offshore Red Sea ridge becomes on-land, to ~ 18 mm/yr in central Afar (Figure 1a) (Eagles et al., 2002; McClusky et al., 2010; Viltres et al., 2020). The plate extension in northern Afar is mainly accommodated within narrow (~ 10 – 30 -km wide), en-echelon volcanic segments that mark the currently active plate boundary and where magmatic activity and faulting are focused (Barberi & Varet, 1970; Hayward & Ebinger, 1996) (Figure 1a). At the northern end of Afar, the onland volcanic segments are Jalua, Alid and Dallol, which are characterized by relatively small volcanic domes within a 10 km wide NNW-trending graben (Figure 1b) (Battaglia et al., 2021; Nobile et al., 2012; Ruch et al., 2021). South of Dallol, erupted magma volumes increase creating the topographic high of the Erta Ale

ridge. Dallol and other volcanoes of the Erta Ale ridge have been recently magmatically active through dike intrusions, dike-induced normal faulting or dike fed eruptive fissures (Moore et al., 2019; Pagli et al., 2012; Watts et al., 2020). The northern Afar rift is also bounded to the west by the Ethiopian escarpment, where a series of border faults and marginal grabens mark the transition from the ~2 km-high Ethiopian Plateau to the Afar rift floor (Chorowicz, 2005; La Rosa, Keir, et al., 2021; Tortelli et al., 2021; Zwaan et al., 2020).

Local seismicity data from northern Afar are difficult to obtain as the area is remote but recordings from past local seismic networks and the NEIC catalog show that several earthquake swarms occurred between the 1960s to early 2000s near Jalua and Alid with magnitudes reaching ~M5 (Dakin, 1975; Gouin, 1979; Ruch et al., 2021). Most notably, the 1993 Bada seismic sequence occurred in the central graben just to the east of the 2022 sequence (Ruch et al., 2021). Based on the occurrence of ground fractures (Figure 1b), coupled with the spatial and temporal characteristics of the seismicity (Ogubazghi et al., 2004), Ruch et al. (2021) suggested that the 1993 seismic sequence was induced by dike intrusion. More recently, a temporary local seismic network operating in northern Afar between 2011 and 2013 recorded swarms of low-magnitude seismicity at shallow depths of the uppermost 6 km, south of Alid on the eastern side of the graben (Figure 1b) (Illsley-Kemp et al., 2018).

The 2022 seismic sequence was located by the global catalogs (NEIC and EMSC) ~25 km south of Alid volcano, in an area known as the Bada graben (Figure 1b). Here we use InSAR measurements of the seismic sequence to show that the deformation was caused by purely tectonic normal faulting without involvement of magma. We also use seismic waveforms from the nearest stations (FURI and ATD) to better understand the temporal evolution of the seismic sequence.

2. Data Analysis and Results

2.1. InSAR Measurements and Modeling

We processed pre- and co-seismic interferograms from ascending (track 014) and descending (track 079) acquisitions made by the European Space Agency (ESA) satellite Sentinel-1a (Figures 1c–1f and Figure S1 in Supporting Information S1), using the InSAR Scientific Computing Environment (ISCE) software package (Rosen et al., 2012). For the processing, we co-registered the SLCs and removed the topographic phase using a 1 arc-sec (~30 m resolution) Shuttle Radar Topography Mission Digital Elevation Model (SRTM DEM) (Farr et al., 2007). We then filtered residual noise and de-correlation using a Goldstein adaptive power spectral filter with strength of 0.2 (Goldstein & Werner, 1998). Finally, we unwrapped the interferograms using the ICU branch cut algorithm and geocoded them using the 1 arc-sec SRTM DEM.

Satellite acquisitions made at different times during the seismic sequence allow us to discriminate which fault segments moved during the initial and the later part of the sequence (Figures 1c–1e). The earliest co-seismic interferogram spans the time period from 16 December 2022 to 28 December 2022 at 03:08 (UTC) including the M_w 5.5 and a few of the aftershocks but not the mb 4.9 on 28 December at 16:14 UTC. This interferogram shows a deformation pattern consisting of two-lobes on the western flank of the Bada graben, with ~4 fringes (i.e., ~12 cm) of satellite Line-of-Sight (LOS) range increase in the western lobe and over 1 fringe (i.e., ~2.8 cm) of satellite LOS range decrease in the eastern lobe (Figure 1c), consistent with slip of a normal fault dipping to the west. A second co-seismic interferogram spanning the time period from 28 December 2022 to 09 January 2023 hence covering the later part of the seismic sequence (Figure 1d), shows a LOS range increase (~3.0 cm) from a second fault positioned a few km to the northwest. This fringe pattern is consistent with slip on a normal fault dipping to the east and we attribute it to the later part of the sequence, that included the mb 4.9 earthquake on 28 December. Stacking of independent pre-seismic interferograms covering a ~8 month-long time period (from early April to mid-December 2022) show no significant deformation caused by either magmatic or tectonic activity in the Bada graben before 23 December 2022 (Figure S1 in Supporting Information S1).

To explain the observed deformation patterns, we assumed two shear dislocation sources (Okada, 1985) in a conventional elastic half space with a Poisson's ratio of 0.25 and a shear modulus of 30 GPa. First, we constrained the geometry and kinematics of the faults by jointly inverting ascending and descending interferograms covering the entire seismic sequence (Figures 1e and 1f). Then we modeled the co-seismic interferograms of the initial and later part of the sequence separately, as they contain different deformation signals, but we fixed the fault geometries based on the results from the joint inversion. The interferograms were first downsampled with a quadtree algorithm (Figure S2 in Supporting Information S1) (Jonsson et al., 2002) and then inverted for uniform slip on

rectangular fault planes, using a Monte Carlo scheme consisting of a simulated annealing algorithm followed by a quasi-Newton method (Cervelli et al., 2001). Uncertainties on the uniform slip model parameters were also estimated using a Monte Carlo simulation of correlated noise (La Rosa, Pagli, et al., 2021; Wang et al., 2014; Wright et al., 2003). We also inverted for distributed fault slip on rectangular fault patches fixing the fault geometry based on the results from the Monte Carlo modeling and using a least square approach combined with a Laplacian Smoothing operator (Wang et al., 2014).

The uniform slip solution of the joint inversion of descending and ascending InSAR data shows that the entire sequence is well explained by two conjugate faults. The largest fault, on the east, is 10.04 km long, 4 km wide, striking NNW-SSE and dipping 43° WSW with normal dip-slip of 25.1 cm, and some left-lateral strike-slip of 7.8 cm (Figure S3 and Table S1 in Supporting Information S1). Fault parameters are well constrained showing narrow 90% Confidence Intervals (Figure S4 and Table S2 in Supporting Information S1). The smaller fault on the west is ~6.4 km long, strikes ~NS and dips ~58°E with normal dip-slip of 12.5 cm and minor left-lateral slip of 5.7 cm (Figure S3 and Table S1 in Supporting Information S1). The fault width is less well constrained than the other model parameters, probably due to the overlap between deformation signals of the two faults (Figure S5 and Table S3 in Supporting Information S1). Nonetheless, fixing the fault width of 5 km provides a geologically reasonable aspect ratio and a good fit to the observed deformation. The model gives a total RMS misfit of 1.6 and 1.5 cm for the ascending and descending interferograms, respectively (Table S1 in Supporting Information S1), with geodetic moments of M_w 5.6 for the largest fault and M_w 5.4 for the smaller fault. The results of the distributed model show that most of the slip along the largest fault (~40 cm) occurred between 2 and 5 km depth (Figure 2). Conversely, a slip of ~30 cm is accommodated by the smaller fault at shallower depths, 1–4 km. The distributed model decreases the total RMS misfit to ~1.3 cm with the total geodetic moment for the whole sequence corresponding to a single M_w 5.76 event (Figure 2).

We also modeled the initial and later part of the sequence separately assuming uniform slip (Figures S6 and S7 in Supporting Information S1). We find that in the initial part of the seismic sequence, up to 28 December at 03:08 UTC, just the largest fault activated, while between 28 December and 9 January 2023 the majority of deformation occurred along the smaller fault but with some minor normal and left-lateral slip also occurred on the larger fault (Figures S6 and S7 in Supporting Information S1).

2.2. Seismic Measurements and Analyses

In order to place additional constraints on the seismic sequence we analyzed the continuous seismic data from the two closest real-time and publicly available stations (FURI and ATD) (Figure 1). We inspected the data during 20–31 December 2022 and found 10 additional earthquakes at these two stations with time delays between the *P* and *S* waves, and waveform lengths, similar to the earthquakes reported by the NEIC and EMSC. All the earthquakes occur during 26–28 December 2022, with no earthquake observed before the M_w 5.5 mainshock (Figure 3a). We computed M_L from amplitude measurements on simulated Wood-Anderson seismograms of both horizontal component data from ATD and FURI for all 15 earthquakes. We used a distance from the two stations to assume epicenters located at the middle of the InSAR deformation signal, and the distance correction for Ethiopia from Keir et al. (2006). Varying the epicentral distance by ± 5 km in line with the length of the fault zone only changes the computed magnitude by a maximum of ± 0.01 magnitude units. Computed M_L are 5.5, 4.6, and 5.3 for the three earthquakes reported by the NEIC as M_w 5.5, mb 4.6 and M_w 4.9 respectively, and by the EMSC as mb 5.2, 4.6, and 4.9. The two additional earthquakes reported as mb 4.5 by the EMSC return M_L of 4.6 and 4.5. Since our M_L are similar to the independent estimates of magnitude, we compute the seismic moment release through the sequence by assuming a 1:1 relationship between M_L and M_w and then computing M_0 using Hanks and Kanamori (1979). The seismic moment release through time shows major pulses on 26 and 28 December, with a total M_0 of 4.03×10^{17} Nm, equivalent to a single M_w 5.7 event (Figure 3b), broadly consistent with the geodetic model of the whole sequence (Figure 2). In detail, our measurements also suggest that the largest earthquake in the second phase of the sequence (28 December 16:14 mb 4.9) is M_w 5.3, significantly larger than quoted by the NEIC and EMSC, and more consistent with the geodetic moment of the second modeled fault.

To further understand how the seismic sequence relates to the geodetic deformation, we conducted cross correlation of the vertical component seismograms from FURI using the 7 largest earthquakes which also have the best signal quality. We filtered the data between 0.001 and 1 Hz and cross-correlated a 210 s long window including 10 s before the *P* wave onset and then well into the full coda of the waveform (Figure 3c). The earthquakes fall

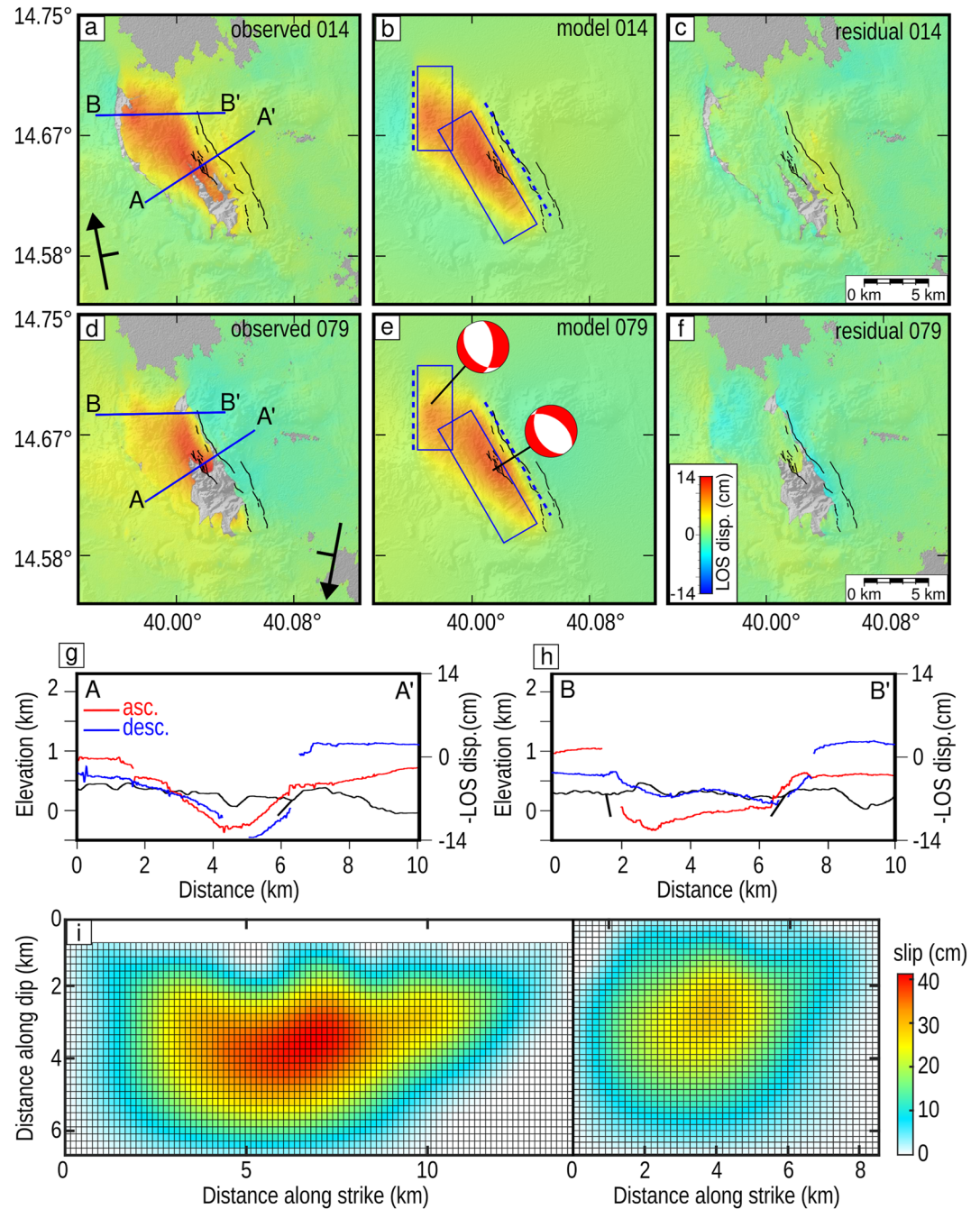


Figure 2. InSAR best-fit distributed slip models for the entire seismic sequence. (a–f) observed, modeled and residual Line-of-Sight (LOS) deformation from joint inversion of ascending and descending tracks. The red beach balls are the geodetic focal mechanisms, blue polygons are the faults outlines. The blue dashed lines are the fault projection at surface while solid lines are the profiles of cross-section shown in (g, h). (g, h) LOS displacement profiles (red and blue lines) across the faults and topographic profile in black (not to scale). Note the change to $-LOS$, thus negative values indicate satellite range increase. (i) Distributed total slip on the fault planes covering the entire seismic sequence. Fault patches are 100×100 m.

into two families of similarity with correlation >0.65 (Figure 3d). Those during the initial part of the sequence correlate well with each other and with the M_w 5.5 mainshock on 26 December, while the earthquakes at the end of the sequence correlate well with each other and with the large earthquake near the end of the sequence on 28 December (Figure 3d). This strongly points toward the two waveform families caused by earthquakes being associated with the two modeled faults, both in terms of location and source mechanism.

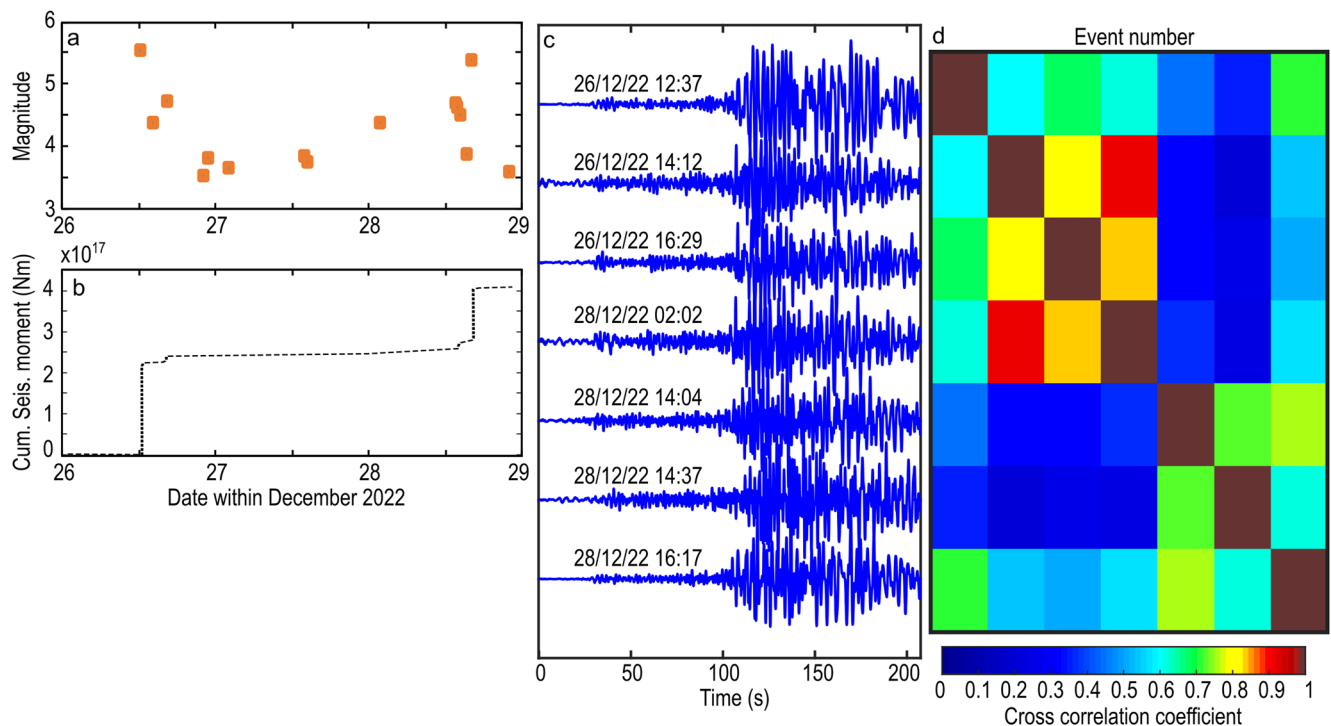


Figure 3. Seismicity in northern Afar in December 2022 as recorded by FURI and ATD. (a) M_L of all 15 earthquakes and (b) cumulative seismic moment release of the seismic sequence. (c) Vertical component waveforms from FURI of the seven largest earthquakes in the December 2022 sequence ordered in chronological order from top to bottom and (d) the associated correlogram. The events on the x and y axes are sorted in chronological order as indicated in panel (c).

3. Discussion

We identified deformation with InSAR in the Bada graben of northern Afar caused by a seismic sequence during 26–28 December 2022. Our modeling shows that the mainshock, M_w 5.5, and aftershocks as far as 28 December at 03:08 (UTC) caused faulting with mainly normal dip-slip on a west dipping plane, while during the later part of the sequence, after 28 December at 03:08 (UTC), a second east dipping fault moved nearby. Overall, during the entire sequence slip occurred on a conjugate normal fault system forming a graben (Figure 2). The geodetic moment for the entire sequence corresponds to M_w 5.76. This agrees with our estimate of seismic moment release from the mainshock and aftershocks which together are equivalent to M_w 5.7. The fact that the sequence is caused by slip on two faults is supported by the observation that all the earthquake waveforms fall into two families of similarity. The first family is similar to the initial mainshock, while the second family is similar to the largest aftershock near the end of the sequence (Figures 3c and 3d). We interpret the earthquakes that occurred up to early on 28 December to have been associated with the initial fault, whereas those from the middle of 28 December to have been associated with slip on the second fault. The results require no significant aseismic component of slip.

Our analysis strongly suggests that the entire seismic sequence was purely tectonic without any involvement of magma and that the fault grew through a tectonically driven mainshock—aftershock sequence. The observed fault slip caused 26 cm of extension, which equates to ~ 30 years of elastic strain accumulation, given the plate extension rate of ~ 9 mm/yr of northern Afar (Viltres et al., 2020). This mode of deformation differs from past geodetically observed occurrences of normal slip earthquakes in Afar which have to date been mainly dike-induced (Nobile et al., 2012; Wright et al., 2012), and therefore directly shows that extensional faults in magma-rich extensional settings can potentially slip without being modulated by magmatic processes. This can potentially be explained by significant along-rift (spatial) variations in magma assisted extension, and/or by temporal variations in supply of magma.

In the Danakil Depression of northernmost Afar, several lines of evidence such as from geomorphology and subsurface seismic reflection imaging point toward along-rift variations in importance of magmatism in extension over the last ~ 100 ka, with faulting dominating extension in regions of an axial graben and with magma

dominating extension where there is the axial volcanic high of the Erta Ale range (Keir et al., 2013). This interpretation is strengthened by the geodetic measurements presented here and over the last 30 years, with past deformation events in the Erta Ale range being dominated by magmatic processes (e.g., Moore et al., 2019; Pagli et al., 2012) while that constrained in our study in the northern graben of the basin lacks magma (Figure 1). Potential reasons for along-rift variations in the contribution of magma toward extension could be along-rift variations in extension rate. In northern Afar, plate spreading is slow (~ 9 mm/yr) compared to the rest of Afar, which in combination with the likely associated lower rates of plate thinning would result in lower rates of decompression melting (Bown & White, 1995), and therefore less magma available to assist rifting. Another explanation is that there are along-rift variations in magma supply caused by segmentation of the upper mantle melt zone such as observed at slow and ultra-slow ocean ridge segments (Phipps Morgan & Chen, 1993; Singh et al., 2006). Under this hypothesis, magma supply would be focused beneath the Erta Ale range, with the segment tips being relatively magma-starved.

Alternatively, since we have only captured a snapshot of the rifting cycle in Afar during the age of space geodesy, it is possible that both mechanisms of tectonic and magma driven faulting occur during magma-assisted rifting at different times. Specifically for the section of the rift near the Bada graben, the involvement of magma in the 1993 sequence and lack of magma in the 2022 sequence points toward the supply of magma not keeping pace with elastic strain accumulation. This explains alternating periods of magma-assisted and magma-starved extension. Alternating magmatic and non-magmatic phases has also been proposed in the Dabbahu volcanic segment. There, significant (up to 3 m) dike-induced fault slip was geodetically observed during 2005–2010, while cosmogenic isotope constraints on the timing of geological fault slip suggest that over the last 100 ka the longer-term fault growth occurred mainly during the periods of suppressed magmatism (i.e., during inter-diking periods) (Medynski et al., 2016). Such evidence is relevant for interpreted fault slip history in northern Afar in that short periods of magmatism may contribute relatively insignificantly to total fault slip.

4. Conclusion

We use InSAR and local seismic recording to better understand an earthquake sequence between 26 and 28 December 2022 in the northern sector of Afar, which started with an M_w 5.5 mainshock. InSAR measurements show that the seismicity was caused by normal faulting alone, without involvement of magma movements such as a dike. Our best-fit InSAR models show that different fault segments of a conjugate system forming a graben ruptured during the seismic sequence with mainly normal dip-slip, corresponding to a single M_w 5.7 event, and in agreement with the seismic moment release from global and local seismic recordings. Our models show that purely tectonic faulting accommodates 26 cm of extension corresponding to ~ 30 years of plate spreading without any link to magma. Our observations show that faults can potentially grow through purely tectonic processes in magma-rich continental rifts. The occurrence of both magma-assisted and purely tectonic fault growth in a single rift can be explained by spatial and/or temporal variations in magma-supply.

Data Availability Statement

The Sentinel-1 IW SLCs and satellite orbits files used in this study are provided by the European Space Agency and can be downloaded through the Copernicus Open Access Hub (<https://scihub.copernicus.eu/dhus/#/>). The InSAR Scientific Computing Environment (ISCE) software package v2 is open source and provided by NASA-JPL at <https://github.com/isce-framework/isce2>. The earthquakes catalogs used in this study are publicly provided by the USGS National Earthquake Information Center (NEIC) and the European Mediterranean Seismological Center (EMSC) and can be downloaded through search forms at <https://earthquake.usgs.gov/earthquakes/search/> and <https://www.emsc-csem.org/#2>. The focal mechanisms used in this study are provided by the global Centroid Moment Tensor Project and can be downloaded at <https://www.globalcmt.org/CMTsearch>. The continuous seismic recordings from FURI and ATD used in this study are publicly available and can be requested to IRIS DMC through the BREQ_FAST form at <http://ds.iris.edu/ds/nodes/dmc/forms/breqfast-request/>. The InSAR dataset and the distributed slip model used in the study are available at the Open Science Framework (OSF) repository via <https://doi.org/10.17605/OSF.IO/7BSVQ> with CC-BY Attribution 4.0 International licence (La Rosa et al., 2023).

Acknowledgments

ALR, CP, DK, MR are supported by Ministero dell'Università e della Ricerca (MiUR) through PRIN Grant 2017P9AT72. HW is supported by the National Natural Science Foundation of China (42274001).

References

Barberi, F., & Varet, J. (1970). The Erta Ale volcanic range (Danakil depression, northern afar, ethiopia). *Bulletin of Volcanology*, 34(4), 848–917. <https://doi.org/10.1007/BF02596805>

Battaglia, M., Pagli, C., & Meuti, S. (2021). The 2008–2010 subsidence of Dallol Volcano on the spreading Erta Ale Ridge: InSAR observations and source models. *Remote Sensing*, 13(10), 1991. <https://doi.org/10.3390/rs13101991>

Bown, J. W., & White, R. S. (1995). Effect of finite extension rate on melt generation at rifted continental margins. *Journal of Geophysical Research*, 100(B9), 18011–18029. <https://doi.org/10.1029/94JB01478>

Cervelli, P., Murray, M. H., Segall, P., Aoki, Y., & Kato, T. (2001). Estimating source parameters from deformation data, with an application to the March 1997 earthquake swarm off the Izu Peninsula, Japan. *Journal of Geophysical Research*, 106(B6), 11217–11237. <https://doi.org/10.1029/2000JB900399>

Chorowicz, J. (2005). The east African rift system. *Journal of African Earth Sciences*, 43(1–3), 379–410. <https://doi.org/10.1016/j.jafrearsci.2005.07.019>

Dakin, F. M. (1975). A preliminary survey of the distribution and characteristics of earthquake sequences in Ethiopia and T.F.A.I. *Bulletin of the Geophysical Observatory of Ethiopia*, 15, 51–70.

Eagles, G., Gloaguen, R., & Ebinger, C. J. (2002). Kinematics of the Danakil microplate. *Earth and Planetary Science Letters*, 203(2), 607–620. [https://doi.org/10.1016/S0012-821X\(02\)00916-0](https://doi.org/10.1016/S0012-821X(02)00916-0)

Ebinger, C. J., Ayele, A., Keir, D., Rowland, J., Yirgu, G., Wright, T., et al. (2010). Length and timescales of rift faulting and magma intrusion: The Afar rifting cycle from 2005 to present. *Annual Review of Earth and Planetary Sciences*, 38(1), 439–466. <https://doi.org/10.1146/annurev-earth-040809-152333>

Farr, T. G., Rosen, P., Caro, E., Crippen, R., Duren, R., Hensley, S., et al. (2007). The shuttle radar topography mission. *Reviews of Geophysics*, 45(2), RG2004. <https://doi.org/10.1029/2005RG000183>

Goldstein, R. M., & Werner, C. L. (1998). Radar interferogram filtering for geophysical applications. *Geophysical Research Letters*, 25(21), 4035–4038. <https://doi.org/10.1029/1998GL900033>

Gouin, P. (1979). *Earthquake history of Ethiopia and the Horn of Africa* (p. 258). International Development Research Centre.

Hanks, T. C., & Kanamori, H. (1979). A moment magnitude scale. *Journal of Geophysical Research*, 84(B5), 2348–2350. <https://doi.org/10.1029/JB084iB05p02348>

Hayward, N. J., & Ebinger, C. J. (1996). Variations in the along-axis segmentation of the Afar. *Tectonics*, 15(2), 1–14. <https://doi.org/10.1029/95TC02292>

Illsley-Kemp, F., Keir, D., Bull, J. M., Gernon, T. M., Ebinger, C., Ayele, A., et al. (2018). Seismicity during continental breakup in the Red Sea rift of Northern Afar. *Journal of Geophysical Research: Solid Earth*, 123(3), 2345–2362. <https://doi.org/10.1002/2017JB014902>

Jonsson, S., Zebker, H., Segall, P., & Amelung, F. (2002). Fault slip distribution of the 1999 M_w 7.1 Hector Mine, California, Earthquake, estimated from satellite radar and GPS measurements. *Bulletin of the Seismological Society of America*, 92(4), 1377–1389. <https://doi.org/10.1785/0120000922>

Keir, D., Bastow, I. D., Pagli, C., & Chambers, E. L. (2013). The development of extension and magmatism in the Red Sea Rift of Afar. *Tectonophysics*, 607, 98–114. <https://doi.org/10.1016/j.tecto.2012.10.015>

Keir, D., Stuart, G. W., Jackson, A., & Ayele, A. (2006). Local earthquake magnitude scale and seismicity rate for the Ethiopian rift. *Bulletin of the Seismological Society of America*, 96(6), 2221–2230. <https://doi.org/10.1785/0120060051>

La Rosa, A., Keir, D., Doubre, C., Sani, F., Corti, G., Leroy, S., et al. (2021). Lower crustal earthquakes in the March 2018 sequence along the Western Margin of Afar. *Geochemistry, Geophysics, Geosystems*, 22(4), e2020GC009614. <https://doi.org/10.1029/2020GC009614>

La Rosa, A., Pagli, C., Wang, H., Ayele, A., Keir, D., & Raggiunti, M. (2023). InSAR data and model of the Bada 2022 seismic sequence (Ethiopia) [Dataset]. Open Science Framework. <https://doi.org/10.17605/OSF.IO/7BSVQ>

La Rosa, A., Pagli, C., Wang, H., Doubre, C., Leroy, S., Sani, F., et al. (2021). Plate-boundary kinematics of the Afrera linkage zone (Afar) from InSAR and seismicity. *Journal of Geophysical Research: Solid Earth*, 126(5), e2020JB021387. <https://doi.org/10.1029/2020JB021387>

McClusky, S., Reilinger, R., Ogubazghi, G., Amleson, A., Healeb, B., Vernant, P., et al. (2010). Kinematics of the southern Red Sea–Afar triple junction and implications for plate dynamics. *Geophysical Research Letters*, 37(5), L05301. <https://doi.org/10.1029/2009GL014127>

Medynski, S., Pik, R., Burnard, P., Dumont, S., Grandin, R., Williams, A., et al. (2016). Magmatic cycles pace tectonic and morphological expression of rifting (Afar depression, Ethiopia). *Earth and Planetary Science Letters*, 446, 77–88. <https://doi.org/10.1016/j.epsl.2016.04.014>

Moore, C., Wright, T., Hooper, A., & Biggs, J. (2019). The 2017 eruption of Erta 'Ale Volcano, Ethiopia: Insights into the shallow axial plumbing system of an incipient mid-ocean ridge. *Geochemistry, Geophysics, Geosystems*, 20(12), 5727–5743. <https://doi.org/10.1029/2019GC008692>

Nobile, A., Pagli, C., Keir, D., Wright, T. J., Ayele, A., Ruch, R., & Accolla, V. (2012). Dike-fault interaction during the 2004 Dallol intrusion at the northern edge of the Erta Ale ridge (Afar, Ethiopia). *Geophysical Research Letters*, 39(19), L19305. <https://doi.org/10.1029/2012GL053152>

Ogubazghi, G., Ghebream, W., & Havskov, J. (2004). Some features of the 1993 Bada earthquake swarm of southeastern Eritrea. *Journal of African Earth Sciences*, 38(2), 135–143. <https://doi.org/10.1016/j.jafrearsci.2003.12.002>

Okada, Y. (1985). Surface deformation due to shear and tensile faults in a half-space. *Bulletin of the Seismological Society of America*, 75(4), 1135–1153. <https://doi.org/10.1785/BSSA0750041135>

Pagli, C., Wright, T. J., Ebinger, C. J., Yun, S. H., Cann, J. R., Barnie, T., & Ayele, A. (2012). Shallow axial magma chamber at the slow-spreading Erta Ale Ridge. *Nature Geoscience*, 5(4), 284–288. <https://doi.org/10.1038/ngeo1414>

Phipps Morgan, J., & Chen, Y. (1993). Dependence of ridge-axis morphology on magma supply and spreading rate. *Nature*, 364(6439), 706–708. <https://doi.org/10.1038/364706a0>

Rosen, P. A., Gurrrola, E. M., Sacco, G. F., & Zebker, H. (2012). The InSAR scientific computing environment. In *ENUSAR; 9th European conference on synthetic aperture radar* (pp. 730–733).

Ruch, J., Keir, D., Passarelli, L., Di Giacomo, D., Ogubazghi, G., & Jónsson, S. (2021). Revealing 60 years of earthquake swarms in the southern Red Sea, Afar and the Gulf of Aden. *Frontiers of Earth Science*, 9, 664673. <https://doi.org/10.3389/feart.2021.664673>

Sigmundsson, F., Hooper, A., Hreinsdóttir, S., Vogfjörð, K. S., Ófeigsson, B. G., Heimisson, E. L., et al. (2015). Segmented lateral dyke growth in a rifting event at Bárðarbunga volcanic system, Iceland. *Nature*, 517(7533), 191–195. <https://doi.org/10.1038/nature14111>

Singh, S., Crawford, W., Carton, H., Seher, T., Combier, V., Cannat, M., et al. (2006). Discovery of a magma chamber and faults beneath a Mid-Atlantic Ridge hydrothermal field. *Nature*, 442(7106), 1029–1032. <https://doi.org/10.1038/nature05105>

Tortelli, G., Gioncada, A., Pagli, C., Rosi, M., De Dosso, L., & Keir, D. (2021). Evidence of active magmatic rifting at the Ma'Alalta volcanic field (Afar, Ethiopia). *Bulletin of Volcanology*, 83(6), 38. <https://doi.org/10.1007/s00445-021-01461-4>

Viltres, R., Jónsson, S., Ruch, J., Doubre, C., Reilinger, R., Floyd, M., & Ogubazghi, G. (2020). Kinematics and deformation of the southern Red Sea region from GPS observations. *Geophysical Journal International*, 221(3), 2143–2154. <https://doi.org/10.1093/gji/ggaa109>

- Wang, H., Elliott, J. R., Craig, T. J., Wright, T. J., Liu-Zeng, J., & Hooper, A. (2014). Normal faulting sequence in the Pumqu-Xainza Rift constrained by InSAR and teleseismic body-wave seismology. *Geochemistry, Geophysics, Geosystems*, *15*(7), 2947–2963. <https://doi.org/10.1002/2014GC005369>
- Watts, E. J., Gernon, T. M., Taylor, R., Keir, d., Siegburg, M., Jarman, J., et al. (2020). Evolution of the Alu-Dalafilla and Borale volcanoes, Afar, Ethiopia. *Journal of Volcanology and Geothermal Research*, *408*, 107094. <https://doi.org/10.1016/j.jvolgeores.2020.107094>
- Wolfenden, E., Ebinger, C., Yirgu, G., Renne, P. R., & Kelley, S. P. (2005). Evolution of a volcanic rifted margin: Southern Red Sea, Ethiopia. *Geological Society of America Bulletin*, *117*(7–8), 846–864. <https://doi.org/10.1130/B25516.1>
- Wright, T. J., Lu, Z., & Wicks, C. (2003). Source model for the M_w 6.7, 23 October 2002, Nenana mountain earthquake (Alaska) from InSAR. *Geophysical Research Letters*, *30*(18), 1974. <https://doi.org/10.1029/2003GL018014>
- Wright, T. J., Sigmundsson, F., Pagli, C., Belachew, M., Hamling, I. J., Brandsdóttir, B., et al. (2012). Geophysical constraints on the dynamics of spreading centres from rifting episodes on land. *Nature Geoscience*, *5*(4), 242–250. <https://doi.org/10.1038/ngeo1428>
- Zwaan, F., Corti, G., Sani, F., Keir, D., Muluneh, A., Illsley-Kemp, F., & Papini, M. (2020). Structural analysis of the Western Afar Margin, East Africa: Evidence for multiphase rotational rifting. *Tectonics*, *39*(7), e2019TC006043. <https://doi.org/10.1029/2019tc006043>